Carbon 172 (2021) 720–728

Contents lists available at ScienceDirect

Carbon

journal homepage: www.elsevier.com/locate/carbon

Research Article

High-response heterojunction phototransistor based on vertically grown graphene nanosheets film

Xi Zhang , Lulu Tian , Dongfeng Diao *

Institute of Nanosurface Science and Engineering, Guangdong Provincial Key Laboratory of Micro/Nano Optomechatronics Engineering, Shenzhen University, Shenzhen, 518060, China

ARTICLE INFO

Article history:
Received 11 June 2020
Received in revised form
29 September 2020
Accepted 18 October 2020
Available online 22 October 2020

Keywords:
Phototransistor
GNEC film
High photoresponsivity
Graphene edge pump
Rapid response
Heterojunction

ABSTRACT

Carbon-phototransistor with a structure of vertically grew graphene nanosheets embedded carbon (GNEC) film is fabricated through an electron-assisted sputtering-deposition method. This heterojunction phototransistor of GNEC/n-Si exhibits broad detection range (from 450 nm to 1200 nm), high photoresponsivity (1.298×10^4 A/W), and rapid response to on-off optical signals (4.91 μs). Driven by the source-drain voltage applied to the GNEC film, electrons recycle in the circuit before recombination, which enhance drastically the usage efficiency of photo-induced carriers. Besides, GNEC film contains a large amount of graphene edges, which may serve as electron pump in the photovoltaic process based on the *e-h* separation in the p-n junction. The GNEC/n-Si phototransistor improves the responsivity of ~10^3 order compared with that of photodiode mode.

1. Introduction

Graphene and other 2D materials have emerged as promising photodetectors because of their fast transport speed [1], broadband response [2,3], band-gap engineering [4], etc. Among various structures, phototransistor has the advantage of fast response [5] and gate modulations [6]. However, phototransistor based on pure graphene exhibited low responsivity(R) due to the lack of electron trapping centers. Therefore, graphene heterojunction combined with other 2D materials [7], perovskite [8], quantum dot [9] and silicon [10] have been explored. Among them, graphene/Si heterojunction is simple and efficient [11–14] and the high-performance graphene/silicon phototransistor had been achieved [14]. These phototransistors are based on chemically vapor deposited (CVD) or mechanically exfoliated graphene. Thus, the fabrication processes are expensive and complicated. In addition, they showed strong dark currents (>10^{-3} A) because of the ultra-high conductivities of CVD graphene or perfect graphene, limiting their applications in photodetection. Therefore, it is necessary to develop a cheap and convenient technique for fabricating high-performance phototransistors.

On the other hand, carbon films deposited by sputtering techniques have the potential for wafer-level-production due to its large deposition area (up to 8 inch), fast growing rate and simple target. But the traditional amorphous carbon (a-C) films exhibit low photoresponsivity below 0.2 A/W [15]. Recently, graphene nanosheets(GNs) embedded carbon (GNEC) films was fabricated by electron-assisted sputtering technique [16]. GNEC films consist of high density of standing structured GNs [17], which have excellent properties in tribology [18] and strong magnetic properties [19].

Herein, we proposed a GNEC film/silicon phototransistor fabricated through an electron-assisted sputtering-deposition method electron cyclotron resonance (ECR) sputtering technique. GNEC film contains a large amount of graphene edges, which serves as electron pump in the photovoltaic process. Different from the photodiode mode adopted in previous studies [16,20], an additional source-drain voltage (V_{SD}) is added on the device. When e-h pair is separated by a photon, the electron will be trapped by graphene edge and driven into the external circuit by V_{SD}. This phototransistor exhibits broad detection range (from 450 nm to 1200 nm), high photoresponsivity (1.298×10^4 A/W), and rapid response to on-off optical signals (4.91 μs).

* Corresponding author.
E-mail address: dfdiao@szu.edu.cn (D. Diao).

https://doi.org/10.1016/j.carbon.2020.10.054
0008-6223/

2. Experimental details

2.1. Samples preparation

GNEC film samples were prepared by ECR plasma sputtering system (see Fig. S1. in the Supporting Information for details). The structure and function of this system were elaborated in our previous reports [16,20]. Several samples were prepared in the ranges of low energy electron irradiation (substrate bias ≤ 80 eV). A microwave power of 500 W was delivered into the chamber to generate a plasma, and a magnetic field was applied to enhance the plasma density. In a high vacuum argon ion (Ar^{+}) plasma atmosphere, carbon atoms from the glassy carbon target are bombarded by plasma ions. Meanwhile, the positive deposition bias (V_{dep} = 80 V) causes electrons to be attracted to the substrate. After acceleration, the active electrons provide the formation energy of sp^2 bonding in the carbon nanostructure. The deposition time was about 15–25min, and the thickness was about 40–70 nm. High density GNs grow vertically on the SiO_2 surface.

2.2. Device preparation

The GNEC films deposited on SiO_2 was immersed in a 10% hydrofluoric acid solution and the sample was transferred. Fig. 1 shows the basic architecture of the GNEC/n-Si phototransistor. Fig. 1(a) illustrates the electrode distribution of GNEC/n-Si heterojunction. The phototransistor, a micron-scale device, has three electrodes: source, drain and gate electrodes [21,22]. The source-drain voltage V_{SD} is applied to the top parallel Au/Ti electrodes. The SiO_2 layer prevents the electric leakage between the electrode and n-Si. The electrode evaporated on the back of device acts as gate voltage (V_{gate}). In Fig. 1(b), a rectangular window was etched to allow the GNEC film contacting with n-Si to form heterojunction. The area of GSEC/n-Si heterojunction is exposed to incidental laser(the effective area of GNEC is 2.3757 mm^2, the laser spot radius is 1.5 mm). A mask was applied to avoid illumination beyond the device. The Lakeshore TTPX low temperature vacuum probe station was used to providing stable bias or current (see Fig. S3 in the Supporting Information for details). The I/V curve of the device was tested in conjunction with a Keithley 4200 semiconductor characterization analyzer under the dark and illuminated conditions.

2.3. Samples morphology

Raman spectroscopy (HORIBA, wavelength of 532 nm) and high-resolution transmission electron microscopy (TEM, FEI Titan3 Themis G2) were used to analyze the characterization of carbon films. Electron energy loss spectrum (EELS, Gatan Quantum ER/965P) was obtained in the TEM system. The EELS was analyzed by deducting the background signal during a baseline alignment processing.

Fig. 2 illustrates the structure of GNEC film and the high-resolution TEM image of GNEC film coated under low-energy electron irradiation at despsition voltatge V_{dep} = 80 V. Fig. 2(a) shows the structure of GNEC film deposited by electron-assisted sputtering technique. Fig. 2(b) is the high resolution TEM image of the cross-section of the sample. It verifies that GNs grow vertically from substrate to top. The thickness of the GNEC film on Si is measured as approximately 53 nm. The top protection layer of metal platinum was deposited only during the preparation of cross-section sample by FIB to protect the film from damages caused by focused ions (see Fig. S2 in Supporting Information for details). Fig. 2(c) is the plan-view TEM of GNEC film. The GNs is marked with the red box, and the regions of amorphous carbon is marked with the green box. In the FFT image of red box, two clearly Laue points appear corresponding to (0001)* facet of multilayer graphene. The reciprocal lattice distance $d^*(0001) = 5.51/2\ nm^{-1} = 2.755\ nm^{-1}$, and the interplanar distance $d = 1/2.755$ nm = 0.363 nm, corresponding to the (0001) facet distance of multilayer graphene. The FFT of a-C marked with the green box shows no Laue points. The embedded GNs in the film are dominated by sp^2, a yellow arrow extends in the direction of the curve from the green illustration of the same scale. The calculated interlayer spacing of the GNs edge is also 0.33 nm through the surface roughness resolution curve. Fig. 2(d) shows the Raman spectrum of the GNEC film. It exhibits obvious *D* and *G* peaks and also 2D peaks. The intensity ratio of *D* peak and *G* peak (I_D/I_G) is 2.36. Unlike the perfect graphene, the intensity of the *D* peak is proportional to the probability of the formation of a hexagonal ring, which means that the crystal structure is ordered. Hence, the high I_D/I_G ratio represents sp^2 hybridized long-range order structure, and a larger number of crystallization occurs in film. Fig. 2(e and f) show the spectrum of EELS under the same condition. The low energy region loss spectrum where the peak at 25 eV illustrates the existence of GNs. The high-energy part of EELS spectrum shows the existence of sp^2 bond. π^* peaks occurs in the vicinity of 285 eV, which indicates the presence of sp^2 bonds. The peak at 292 eV of the σ^* band shows the presence of a crystal structure [23].

3. Results and discussions

3.1. Photo-responsivity performances

Fig. 3 shows the high performance of GNEC/n-Si phototransistor. Fig. 3(a)–(d) show the I_{SD} -V_{SD} curves for various incidental power (P) of GNEC/n-Si at 600 nm, 850 nm, 915 nm and 1000 nm. The electrodes measured are source and drain electrodes in Fig. 1(b). The photocurrent roughly follows the photoconductor characteristic which is roughly symmetric on two sides of V_{SD} = 0 V. The curve is not strictly linear since the transport channel is p-n junction but not a pure conductor. The fluctuation of I–V curves is possibly caused by the noises of the environment, such as the fan in the heat sink of laser. Since the device area is rather small, the noises may causes a tiny vibration of the contact probe to the electrode. Such small fluctuation does not affect the photocurrent measurement and can also be observed in other Van de Waals heterojuction photodetector [24,25]. The dark current at V_{SD} = 2 V is 4.85 μA, while the photocurrent is 0.11 mA under 13.33 μW 600 nm laser. The dark current is in the order of 10^{-6} A since there are a few free electrons and holes in GNEC film driven by V_{SD} to form dark current. Under illumination, e-h were separated by photon excitation and flew into the V_{SD} circuit to form photocurrent. The GNEC/n-Si phototransistor can generate considerable photo-response in the near-infrared region (1000 nm).

Besides, the effects of V_{Gate} on the I_{SD}-V_{SD} curves were investigated. Fig. S4 shows the dependence of I_{SD}-V_{SD} curves and open-circuit voltage (V_{OC}) on the V_{Gate}. Since the conduction channel is a heterojunction in this case, the device is different from the conventional transistor [22]. The V_{Gate} increases the depletion zone of the p-n junction. Hence, it does not enhance the responsivity but change the position of V_{OC}. When V_{Gate} increases from 0 V to 0.5 V, V_{OC} increases from 0 V to 0.34 V.

The Power-dependent photocurrent (source-drain photocurrent) and *R* curves at V_{SD} = 2 V are represented in Fig. 4(a)–(d). The *R* increases from 3801.98 A/W of 1000 nm laser to 1.298×10^4 A/W of 600 nm laser, which *R* at 450 nm is 357 A/W. The phototransistor has a broad detection range (from 450 nm to 1200 nm). The detection range is beyond the normal silicon in the near-infrared region due to the narrower band gap of graphene nanosheets compared with n-type silicon. Fig. 4(a) shows the *R* under 600 nm

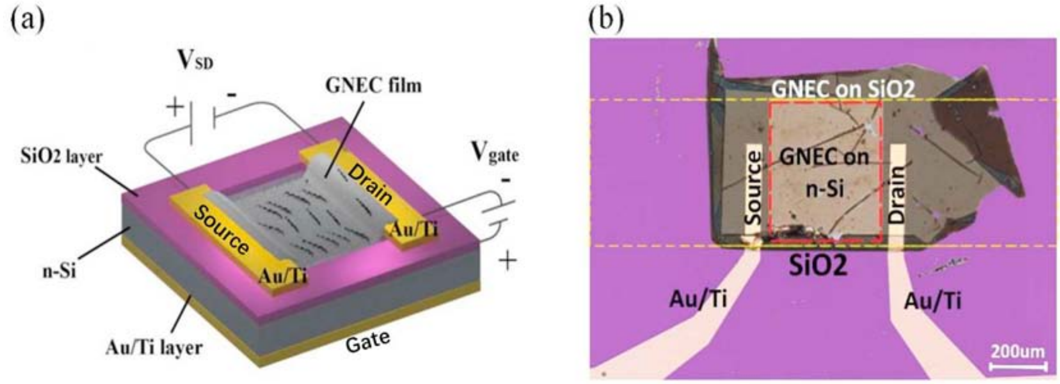

Fig. 1. Illustration of the structure of the GNEC/n-Si phototransistor device. (a) The diagram of the GNEC/n-Si phototransistor device with bias. (b) Top-view optical image of GNEC/n-Si phototransistor device. Source and drain Au/Ti electrodes was fabricated by electron beam lithography (EBL) method. Red window on SiO_2 was etched to allow GNEC film to contact with the n-Si. (A colour version of this figure can be viewed online.)

laser increases from 7.98 to 1.2529 × 10^4 A/W as the incident power P decreases from 13.33 μW to 5.44 nW, while the photocurrent I_{ph} decreases from 0.11 mA to 0.76 μA. Fig. 4(b) shows the R under 850 nm laser increases from 5.21 to 6993.41 A/W as the incident power P decreases from 8.78 μW to 5.44 nW, while the photocurrent I_{ph} decreases from 0.65 μA to 0.38 μA. Fig. 4(c) shows the R under 915 nm laser increases from 4.34 to 7419.76 A/W as the incident power P decreases from 0.13 μW to 5.44 nW, while the photocurrent I_{ph} decreases from 0.58 μA to 0.40 μA. Fig. 4(d) shows the R under 1000 nm laser increases from 7.34 to 3801.98 A/W as the incident power P decreases from 0.13 μW to 5.44 nW, while the photocurrent I_{ph} decreases from 0.11 mA to 0.28 μA. The R at the GNEC film/-Si heterojunction contact interface was calculated with photo-current ($I_{ph} = I_{SD} - I_{dark}$) and P [6] $R = I_{ph}/P$. Fig. 4(e and f) show the contour map of R as a function of V_{SD} (0 V–2 V) and wavelength (450 nm–1200 nm) at P = ~20 nW. The wavelength ranges from 450 to 1200 nm with an interval of 15 nm. The R has the peak of 1.25 × 10^4 A/W at the wavelength of 600 nm (V_{SD} = 2 V). The NEP is 2.236 × 10^{-17} W/$Hz^{1/2}$ and the specific detective D* reaches to 2.836 × 10^{16} Jones (see Table S2 from Supporting Information for details).

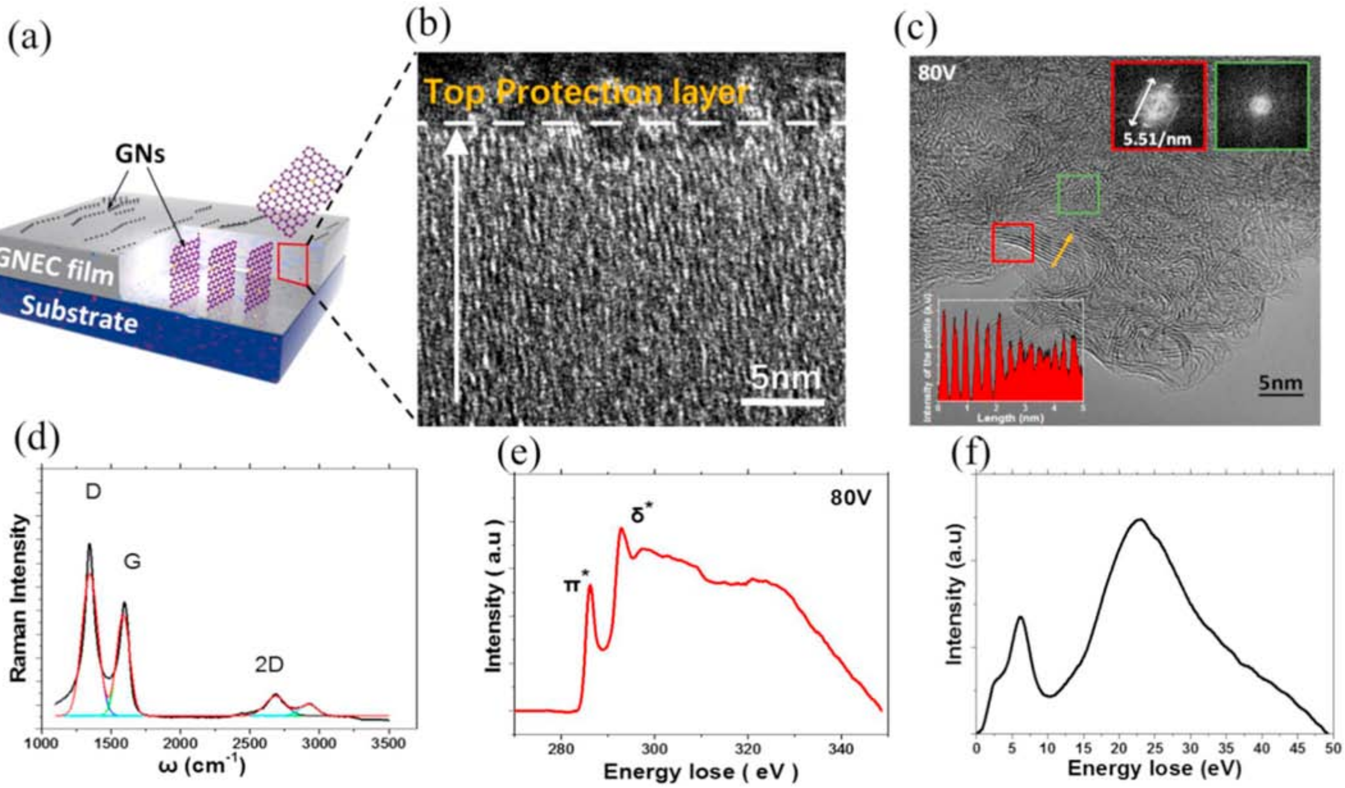

Fig. 2. The film contains a lot of vertically grown GNs embedded in amorphous carbon. (a) The structure diagram of GNEC film. (b) High-resolution TEM micrographs of 80 V GNEC film cross-section sample prepared by focused ion beam (FIB). (c) Plan-view TEM image of GNEC film with V_{dep} = 80 V. Insets show the FFT images and the detailed profile along orange arrow. (d) The Raman spectrum and (e) and (f) The EELS of the GNEC film under the same condition. (A colour version of this figure can be viewed online.)

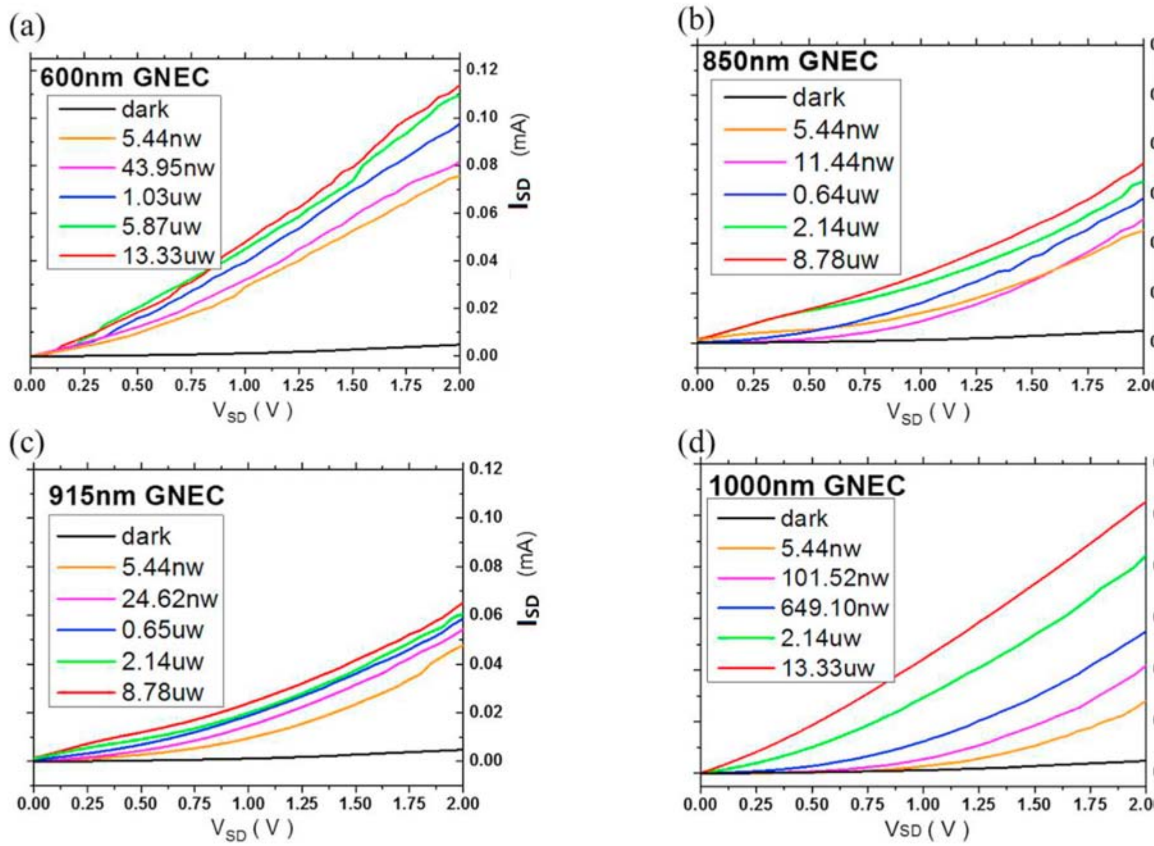

Fig. 3. The photocurrent performance of the GNEC/n-Si phototransistor. (a, b, c, d) I_{SD}-V_{SD} curves for various incidental power of GNEC/n-Si at 600 nm, 850 nm, 915 nm and 1000 nm. (A colour version of this figure can be viewed online.)

3.2. Discussion: p-n junction transistor and possible mechanism

Fig. 5 shows the motion of carriers in the device during the response of the switching pulse signal. Red circles represent negatively charged electrons, and green circles represent positively charged holes. Black dashed circle means the original position of carriers. The device is a p-n junction transistor with three electrodes (source, drain and gate). The conduction channel of the transistor is not a conductor but a p-n junction in this case. Since the light absorption ability of graphene and other carbon materials are not good [26,27], a p-n junction is introduced by n-Si which can improve the light-matter interaction and induce more carriers. The high-performance of the device is mainly due to the p-n junction transistor structure, which drives the photon-separated electrons into the external circuit and electrons recycle in the circuit before recombination. Meanwhile, the graphene edges may possibly serve as electron pumps in the photovoltaic process. Fig. S5 shows the principle of electron trapping at edges of GNs. At a representative monolayer GN, along the width direction, bond length at edges was shortened compared with that of bulk due to the automatically relaxation towards lower energy [28]. The effective atomic potential to neighbor electrons at the edges was lowered compared with those in bulk. In energy space, mid-gap energy states in the vicinity of Fermi-level were generated at edges (edge states) as identified by STM/S experiment [29]. It does not exist only at bare zigzag edge, but also at hydrogen-terminated edges [30], defective edges [30–32] and oxidized edge (see supporting information). Since the potential wells at edges were lowered, they tend to trap itinerate electrons at edges. In GNEC film, a large amount of standing structured GNs provide high density of edges which can serve as electron trapping centers. The edge electron traps are shallow (near the Fermi-level) and hydrogenation-insensitive (as shown in Fig. S5). According to our DFT calculation and the Bond-order-length-strength correlation (BOLS) corrected Hubbard model [28], the edge states of bare zigzag edge and H-zigzag both appear in the vicinity of Fermi-level ($E = 0$). Although the strong dangling δ-bond at zigzag edge can be easily saturated, the localized π-states (p_z electron) which was induced by the local bond contraction and potential well depression, are insensitive to the hydrogenation [28,33]. The theoretical model of edge quantum trapping is stated in supporting information.

Fig. 5(a) illustrates the formation of a heterojunction when no external bias is applied. After the combination of n-type silicon and GNEC film, a potential barrier is spontaneously generated due to the difference in Fermi-energy levels (see band diagram in supporting information). Electrons flew from n-Si to GNEC film due to the high chemical potential of n-Si, and the heterojunction was formed. A built-in electric field (V_{bi}) in the junction area was generated. GN edges store a few electrons and electron-hole pair combines together. Fig. 5(b) shows that in darkness, V_{SD} drives the electrons and holes of GNEC film to flow separately and to form I_{dark}. But the I_{dark} is low since most carrier pairs remain combined. Fig. 5(c and d) describe the high-gain mechanism of the GNEC/n-Si phototransistor mode. The electron-hole separation (Fig. 5(c)) and electron recycling (Fig. 5(d)) happen almost simultaneously under illumination. Fig. 5(c) shows that in incident power condition, the electron-hole pair quickly separates after obtaining photon energy. Electrons and holes flew oppositely across the pn junction due to the built-in voltage V_{bi}. Fig. 5(d) shows that GNs edge pump releases the original electron and stores newly generated electron

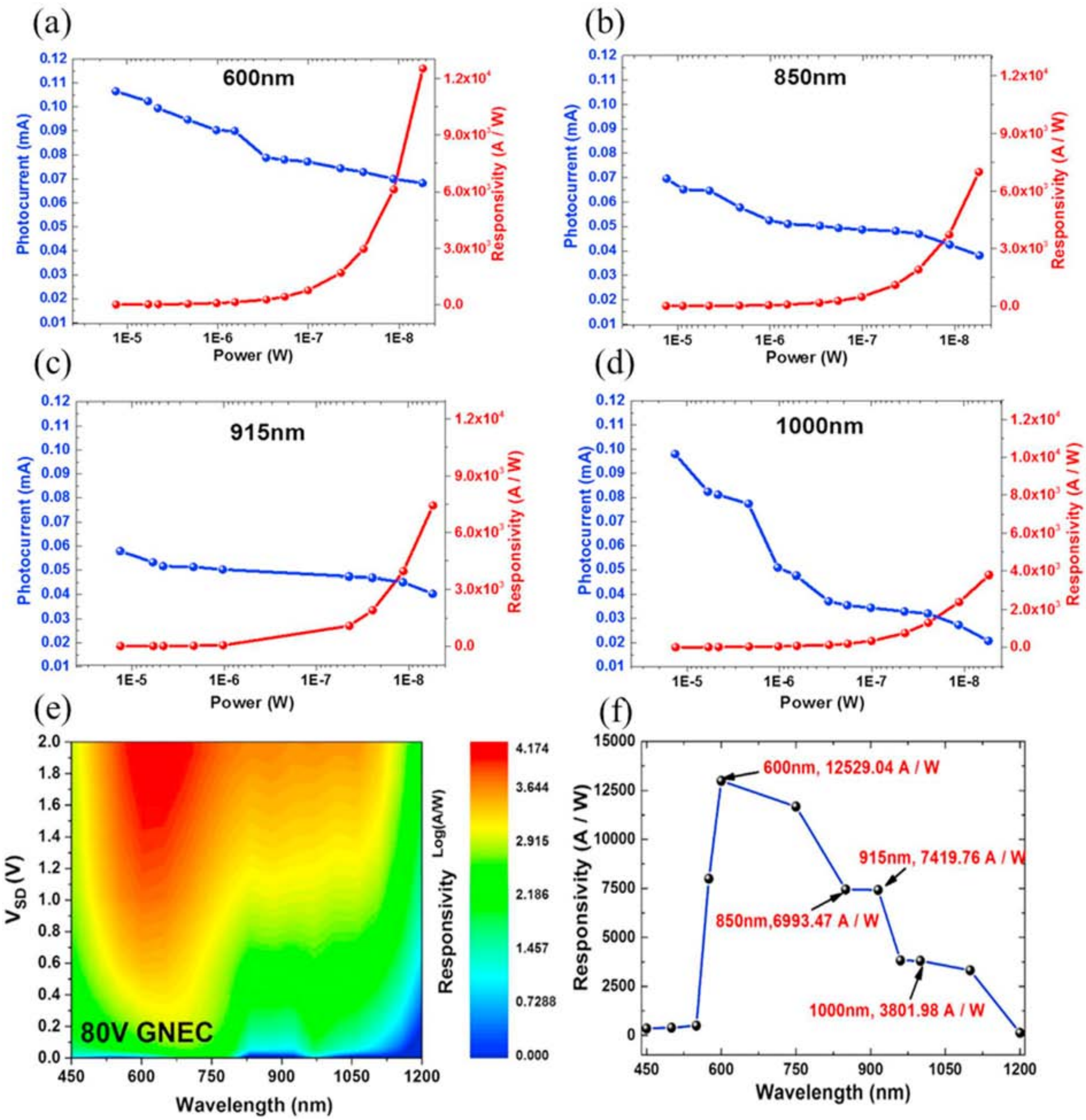

Fig. 4. The photoresponse performance of the GNEC/n-Si phototransistor. (a, b, c, d) At V_{SD} = 2 V, *P*-dependent *R* and source-drain photocurrent (I_{ph}) of GNEC/n-Si at 600 nm, 850 nm, 915 nm and 1000 nm. (e) The contour map of *R* as a function of V_{SD} (0 V–2 V) and wavelength (450 nm–1200 nm, P = ~20 nW). (f) Spectral response at V_{SD} = 2 V of GNEC film. (A colour version of this figure can be viewed online.)

alternatively. In the phototransistor mode, an additional source-drain voltage (V_{SD}) is added on the device. When e-h pair is separated by a photon, the electron will be trapped by graphene edge and driven into the external circuit by V_{SD}. The electrons will recycle in the circuit before recombination due to the ultrafast velocity of electrons and the graphene edges may serve as pumps in this situation. Hence, the *R* of phototransistor mode achieves $>10^4$ improvement compared with the photodiode mode. The incident photon conversion efficiency (IPCE) can be calculated as [13,34].

$$IPCE = \frac{hc(J_{ph} - J_{dark})}{q\lambda P_{in}} \times 100\%$$

where *h, c,* and *q* represents Planck constant, velocity of light, and electron charge, respectively. J_{dark} represents dark current density, and J_{ph} represents photocurrent density. P_{in} represents incident power density. The GNEC/n-Si phototransistor exhibits the photoresponsivity of 1.25×10^4 A/W under the 600 nm laser. According the formula, the IPCE of this situation is 2.58×10^6%. The IPCE exceeds far from 100% was achieved. Fig. 5(e) shows that, when light is off, the separated electrons and holes are gradually recombined into electron-hole pairs.

3.3. Time response

We have tested the dynamic switching response of the device. Frequency response of a 5 kHz optical signal is measured by an oscilloscope, as shown in Fig. 6(a). A diode laser (Coherent OBIS) was modulated on/off with 50% duty cycle by a 5 kHz square waveform generated by a function generator (Keysight 33,600 A).

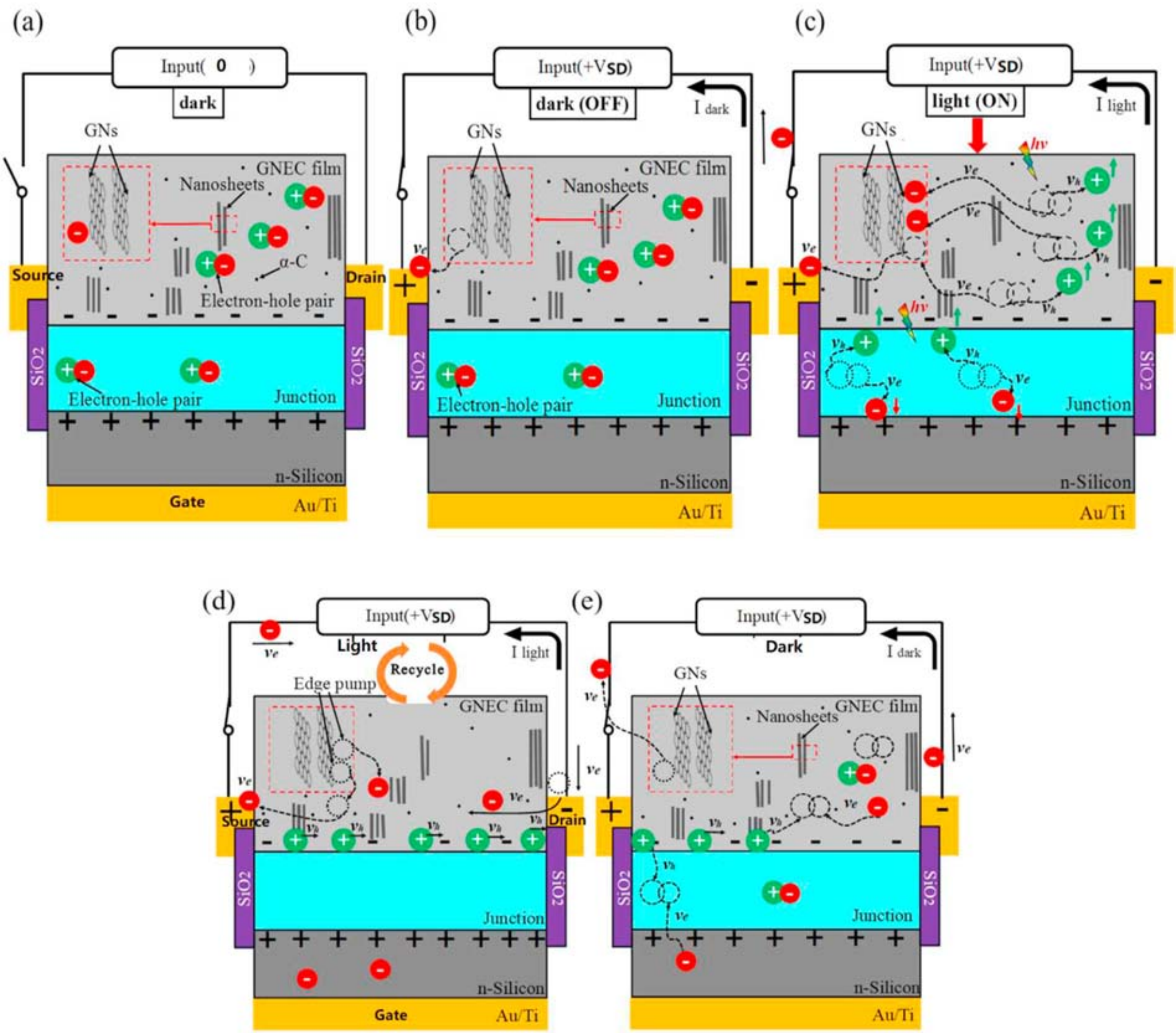

Fig. 5. Possible high-responsivity mechanism of the GNEC/n-Si phototransistor device. (a) Junction formation of GNEC/n-Si transistor. (b) Dark current caused by a few free electrons and holes flow driven by V_{SD}. (c)The electron-hole separation and (d) electron recycling happen almost simultaneously under illumination. (c) A large amount of electron-hole separation under illumination; (d) V_{SD} drives the photon-separated electrons into the external circuit and electrons recycle in the circuit before recombination. GN edges may serve as electron pumps in this process. (e) Part of carriers recombinate when light is off. (A colour version of this figure can be viewed online.)

The rise/fall time of the modulated diode laser was 10 ns. The switching transient response waveform of acquisition device is dependent on the frequency of continuous square wave pulse signal. The OFF pulse signal in Fig. 6(a) corresponds to the V_{SD} in the dark condition in Fig. 5(b).

At the same time with the pulse ON signal, the photo-response voltage of the device increases. Fig. 6(b) shows the rise stage in the rising photo-voltage response which lasts for τ_R. The rising time (τ_R) is as fast as 4.91 μs. The vertical GNs form the electron channels. The photovoltage (red line) of the device affected by a pulsed rise signal as a function of τ by fitting the experimental data with a function, which is written as:

$$I = A \times (1 - \exp(-t / \tau_R)) \quad (1)$$

Fig. 6(c) illustrates the end stage of peak falling edge of the response (τ_D = 26.2 μs). The red lines in Fig. 6(c) is obtained by fitting the experimental data, which is written as:

$$I = A_1 \times \exp(-t / \tau_D) \quad (2)$$

when the incident square wave signal is 5 kHz, the rising peak and the falling peak edge generate in synchronization.

In Fig. 6(a), it can be seen that the response curve has a capacitive effect, i.e. the photovoltage increases to a high value when light is just on and falls down gradually during the ON period. That is due to the pn junction inside the device serving as a capacity. The excellent light-conducting properties allow the device to maintain the accurate and stable switching performance at room temperature. Since the built-in potential difference generated in the heterojunction has an efficient isolation operation for light-induced electron-hole pairs, the lifetime of carrier recombination is prolonged [6]. The electron tunnel probability gradually decreases as the built-in barrier thickness decreases.

3.4. Comparisons

Fig. 7 shows the comparison of performance with previous photodetectors (see Table S2 in the Supporting Information for details), such as SWIR(Graphene photodetectors) [35], GNEC film/p-Si [16], Schottky-graphene/Si heterojunction [36], Tunable

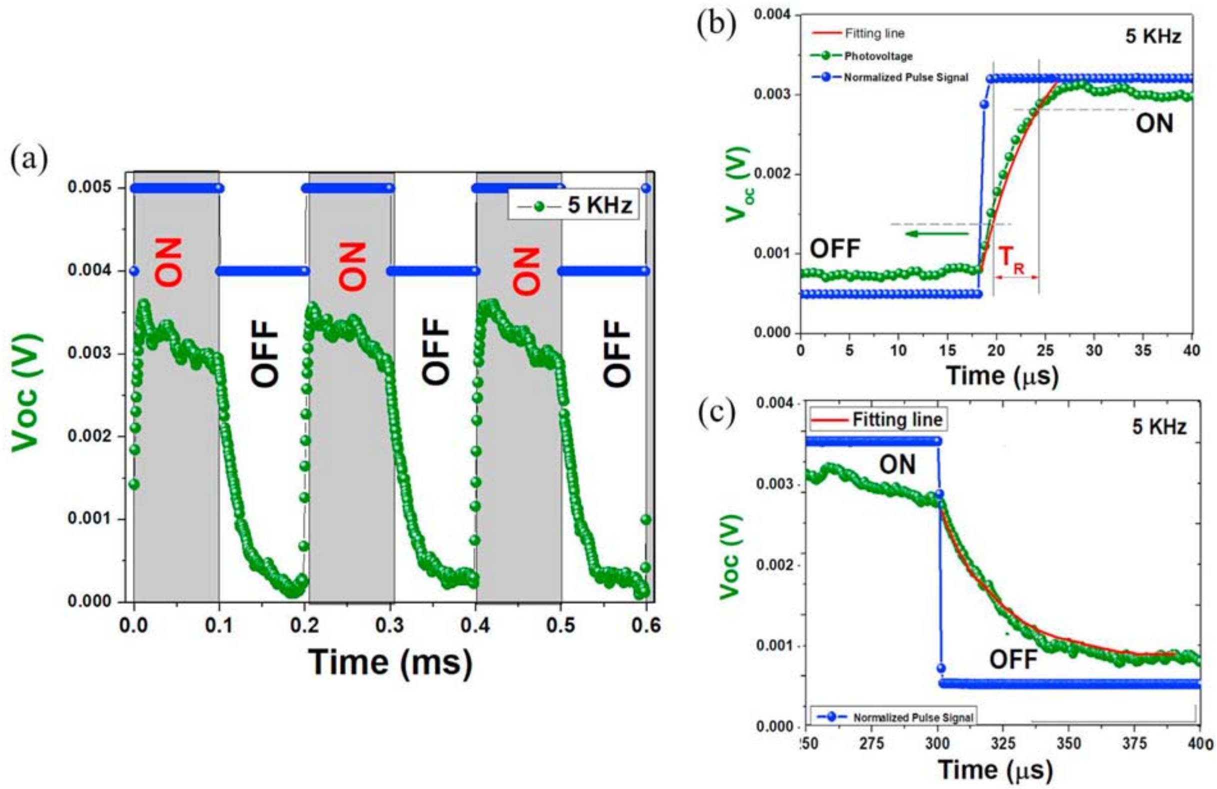

Fig. 6. Response time for laser beams with a repeated frequency of 5 kHz. (a) Frequency response of a 5 kHz optical signal of 100 mW under laser illumination. The V_{OC} signal is over 3 ON/OFF periods. (b–c) The enlarged views of the photocurrent response in the rise and fall period. (A colour version of this figure can be viewed online.)

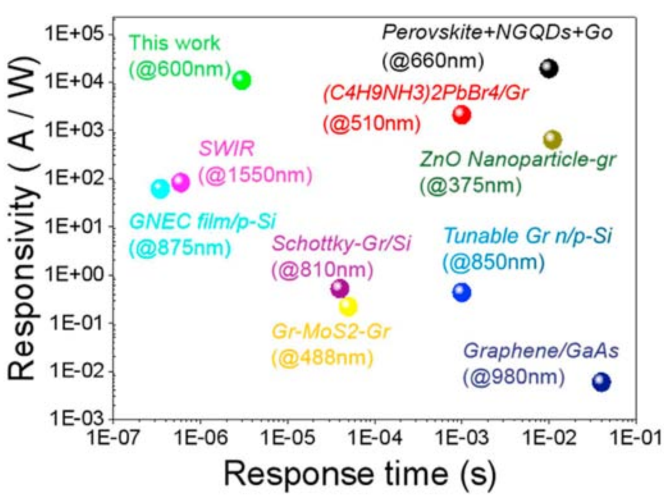

Fig. 7. The dependence of the *R* on the response time (τ_{rise}) of our device, compared with those of typical reported hybrid graphene photodetector/phototransistors including other materials (e.g. ZnO, GaAs, MoS2, perovskite). The corresponding reference number (in square brackets) and the peak wavelength (in parentheses) are labelled in respective text. (A colour version of this figure can be viewed online.)

Graphene n/p-Si [37], Perovskite + NGQDs + GO [38], $(C_4H_9NH_3)_2PbBr_4$/Graphene [8], ZnO Nanoparticle-Graphene [39], Graphene/GaAs [40], and Graphene-MoS_2-Graphene [41]. Graphene/Si heterojunctions photodiode has responsivity of 11 A/W [14,37]. Phototransistor with a structure of a nitrogen-doped graphene quantum dots (NGQDs)–perovskite composite layer and a mildly reduced graphene oxide (mr GO) layer, exhibits high photoresponsivity (1.92 × 10^4 A/W), and response time to ON–OFF(≈10 ms) [38]. The ZnO nanoparticle–graphene core–-shell structures shows an maximum photoresponsivity 640 A/W at 375 nm, the response time (<1 ms) [39]. 2D $(C_4H_9NH_3)_2PbBr_4$ perovskite/graphene photodetector at a wavelength of 510 nm shows high responsivity (~2100 A/W) [8]. Self-driven graphene/GaAs has *R* 5.97 mAW^{-1} and corresponding detectivity is 1.1 × 10^{11} $cmHz^{0.5}W^{-1}$ [40]. Graphene–MoS_2–graphene layer device has the photocurrent external quantum efficiency of 55% (corresponding to a photoresponsivity of 0.22 A W^{-1}) at wavelength of 488 nm [41]. The performance (R = 1.2 × 10^4 A/W and τ = 4.91 μs) of this work is outstanding among the references.

Unlike the plane graphene, high-density GNs in GNEC film plays an important role in carrier transport. Vertically structure of GNs exert the ability of graphene edge quantum traps capturing and retaining carriers. Compared with the GNEC/n-Si [20] and GNEC/p-Si [16] photodiode in previous reports, the device in this manuscript is a phototransistor. In the previous photodiode mode, there are only two electrodes - GNEC film and Si substrate. The photo-separated electrons and holes drift oppositely through the p-n junction due to the built-in electric field, to form the photocurrent. In contrast, in the phototransistor mode in this work, an additional V_{SD} is added on the device. When e-h pair is separated by a photon, the electron will be trapped by graphene edge and driven into the external circuit by V_{SD}. The electrons will recycle in the circuit before recombination due to the ultrafast velocity of electrons and the graphene edges serves as pumps in this situation. Hence, the responsivity of phototransistor mode achieves huge improvement. Besides, the difference between the GNEC/p-Si and the GNEC/n-Si mainly come from the formation of the p-n junction with or without external bias (see Table S3).

4. Conclusions

In summary, we have resolved the GNEC films with a three-dimensional structure in which high-density vertical GNs are embedded between a-C. A large number of electrons recycled in the V_{SD} circuit before recombination based on the *e-h* separation in the p-n junction. It enhances drastically the usage efficiency of photo-electrons. Compared with GNEC/Si diode and other graphene 2D materials photovoltaic detectors, the GNEC/n-Si phototransistor shows markedly outstanding performance. The highest photo-responsivity can reach to 1.298×10^4 A/W at 600 nm. The hetero-junction phototransistor exhibits broad detection ranging from 450 nm to 1200 nm. Fast response time of 4.91 μs is achieved as well. The change of the gate-voltage affects the V_{OC} of the device. In addition to the separation of the photo-generated carriers due to the built-in potential field of the p-n junction, the V_{SD} voltage increases the total transport of carriers. This research provides a wafer-level-produced and low-cost preparation idea for future in-depth research on weak detection.

CRediT authorship contribution statement

Xi Zhang: Conceptualization, Methodology, Investigation, Writing - original draft. **Lulu Tian:** Investigation, Data curation, Writing - original draft. **Dongfeng Diao:** Conceptualization, Supervision, Project administration.

Declaration of competing interest

The authors declare that they have no known competing financial interests or personal relationships that could have appeared to influence the work reported in this paper.

Acknowledgements

The work was supported by National Natural Science Foundation of China (No. 51605306) of China and Shenzhen Overseas High-level Talents Innovation and Entrepreneurship Plan (No.KQJSCX20180328094853770). Thank Mr. Xiaolin Li and Mr. Zezhou Lin for designing the cover art.

Appendix A. Supplementary data

Supplementary data to this article can be found online at https://doi.org/10.1016/j.carbon.2020.10.054.

References

[1] J. Mao, Y. Yu, L. Wang, X. Zhang, Y. Wang, Z. Shao, et al., Ultrafast, broadband photodetector based on MoSe2/silicon heterojunction with vertically standing layered structure using graphene as transparent electrode, Adv. Sci. 3 (2016) 1600018.
[2] Y. Zhang, T. Liu, B. Meng, X. Li, G. Liang, X. Hu, et al., Broadband high photoresponse from pure monolayer graphene photodetector, Nat. Commun. 4 (2013) 1811.
[3] L. Hao, Y. Du, Z. Wang, Y. Wu, H. Xu, S. Dong, et al., Wafer-size growth of 2D layered SnSe films for UV-Visible-NIR photodetector arrays with high responsitivity, Nanoscale 12 (2020) 7358–7365.
[4] W. Zhang, J.-K. Huang, C.-H. Chen, Y.-H. Chang, Y.-J. Cheng, L.-J. Li, High-gain phototransistors based on a CVD MoS2 monolayer, Adv. Mater. 25 (2013) 3456–3461.
[5] Q. Huang, D. Zeng, H. Li, C. Xie, Room temperature formaldehyde sensors with enhanced performance, fast response and recovery based on zinc oxide quantum dots/graphene nanocomposites, Nanoscale 4 (2012) 5651–5658.
[6] Z. Chen, Z. Cheng, J. Wang, X. Wan, C. Shu, H.K. Tsang, et al., High responsivity, broadband, and fast graphene/silicon photodetector in photoconductor mode, Advanced Optical Materials 3 (2015) 1207–1214.
[7] L. Yu, Y.H. Lee, X. Ling, E.J. Santos, Y.C. Shin, Y. Lin, Graphene/MoS2 hybrid technology for large-scale two-dimensional electronics, Nano Lett. 14 (2014) 3055.
[8] Z. Tan, Y. Wu, H. Hong, J. Yin, J. Zhang, L. Lin, et al., Two-dimensional (C4H9NH3)2PbBr4 perovskite crystals for high-performance photodetector, J. Am. Chem. Soc. 138 (2016) 16612–16615.
[9] X. Liu, W. Kuang, H. Ni, Z. Tao, Q. Huang, J. Chen, A highly sensitive and fast graphene nanoribbon/CsPbBr3 quantum dot phototransistor with enhanced vertical metal oxide heterostructures, Nanoscale 10 (2018) 10182–10189.
[10] F.L.X. An, Y.J. Jung, S. Kar, Tunable graphene-silicon heterojunctions for ultrasensitive photodetection, Nano Lett. (2003) 909–916.
[11] S. Kobayashi, Y. Anno, K. Takei, T. Arie, S. Akita, Photoresponse of graphene field-effect-transistor with n-type Si depletion layer gate, Sci. Rep. 8 (2018) 4811.
[12] L. Tao, Z. Chen, X. Li, K. Yan, J.-B. Xu, Hybrid graphene tunneling photoconductor with interface engineering towards fast photoresponse and high responsivity, npj 2D Materials and Applications 1 (2017) 19.
[13] X. Wan, Y. Xu, H. Guo, K. Shehzad, A. Ali, Y. Liu, et al., A self-powered high-performance graphene/silicon ultraviolet photodetector with ultra-shallow junction: breaking the limit of silicon? npj 2D Materials and Applications 1 (2017) 4.
[14] A. Hekmatikia, Y. Abdi, Graphene–silicon-based high-sensitivity and broad-band phototransistor, IEEE Electron. Device Lett. 39 (2018) 216–219.
[15] K.M. Krishna, M. Umeno, Y. Nukaya, T. Soga, T. Jimbo, Photovoltaic and spectral photoresponse characteristics of n-C/p-C solar cell on a p-silicon substrate, Appl. Phys. Lett. 77 (2000) 1472–1474.
[16] Xi Zhang, Zezhou Lin, Da Peng, Lei Ye, Jianfeng Zang, D. Diao, Edge-State-Enhanced ultrahigh photoresponsivity of graphene nanosheet-embedded carbon film/silicon heterojunction, Adv. Mater. Interfaces 6 (2019) 1802062–1802071.
[17] X. Zhang, D. Peng, Z. Lin, W. Chen, D. Diao, Edge effect on the photodetection ability of the graphene nanocrystallites embedded carbon film coated on p-silicon, Phys. Status Solidi Rapid Res. Lett. 13 (2019) 201800511.
[18] L. Yang, K. Qi, D. Diao, P. Wang, P. Xue, Magnetostrictive friction of graphene sheets embedded carbon film, Carbon 159 (2020) 617–624.
[19] C. Wang, X. Zhang, D. Diao, Nanosized graphene crystallite induced strong magnetism in pure carbon films, Nanoscale 7 (2015) 4475–4481.
[20] X. Zhang, Z. Lin, D. Peng, D. Diavdo, Bias-modulated high photoelectric response of graphene-nanocrystallite embedded carbon film coated on n-silicon, Nanomaterials 9 (2019) 327.
[21] Z. Wang, J. Liu, X. Hao, Y. Wang, Y. Chen, P. Li, et al., Investigating the stability of molecule doped graphene field effect transistors, New J. Chem. 43 (2019) 15275–15279.
[22] Y. Hong, S. Wang, Q. Li, X. Song, Z. Wang, X. Zhang, et al., Interfacial icelike water local doping of graphene, Nanoscale 11 (2019) 19334–19340.
[23] X. Fan, D. Diao, Ion excitation and etching effects on top-surface properties of sp2 nanocrystallited carbon films, Appl. Surf. Sci. 462 (2018) 669–677.
[24] S. Zhao, J. Wu, K. Jin, H. Ding, T. Li, C. Wu, et al., Highly polarized and fast photoresponse of black phosphorus-InSe vertical p-n heterojunctions, Adv. Funct. Mater. 28 (2018) 1802011.
[25] M. Massicotte, P. Schmidt, F. Vialla, K.G. Schädler, A. Reserbat-Plantey, K. Watanabe, et al., Picosecond photoresponse in van der Waals heterostructures, Nat. Nanotechnol. 11 (2016) 42–46.
[26] F. Xia, T. Mueller, Y.-M. Lin, A. Valdes-Garcia, P. Avouris, Ultrafast graphene photodetector, Nat. Nanotechnol. 4 (2009) 839–843.
[27] M. Furchi, A. Urich, A. Pospischil, G. Lilley, K. Unterrainer, H. Detz, et al., Microcavity-integrated graphene photodetector, Nano Lett. 12 (2012) 2773–2777.
[28] X. Zhang, Y. Nie, W. Zheng, J.-L. Kuo, C.Q. Sun, Discriminative generation and hydrogen modulation of the Dirac-Fermi polarons at graphene edges and atomic vacancies, Carbon 49 (2011) 3615–3621.
[29] T. Enoki, Y. Kobayashi, K.-I. Fukui, Electronic structures of graphene edges and nanographene, Int. Rev. Phys. Chem. 26 (2007) 609–645.
[30] Y. Kobayashi, K.-I. Fukui, T. Enoki, K. Kusakabe, Edge state on hydrogen-terminated graphite edges investigated by scanning tunneling microscopy, Phys. Rev. B 73 (2006) 125415.
[31] Y. Niimi, T. Matsui, H. Kambara, K. Tagami, M. Tsukada, H. Fukuyama, Scanning tunneling microscopy and spectroscopy of the electronic local density of states of graphite surfaces near monoatomic step edges, Phys. Rev. B 73 (2006), 085421.
[32] M.M. Ugeda, I. Brihuega, F. Guinea, J.M. Gomez-Rodriuez, Missing atom as a source of carbon magnetism, Phys. Rev. Lett. 104 (2010), 096804.
[33] X. Zhang, C. Wang, C.Q. Sun, D. Diao, Magnetism induced by excess electrons trapped at diamagnetic edge-quantum well in multi-layer graphene, Appl. Phys. Lett. 105 (2014), 042402.
[34] F. Liu, S. Kar, Quantum Carrier Reinvestment-induced ultrahigh and broad-band photocurrent responses in graphene-silicon junctions, ACS Nano 8 (2014) 10270–10279.
[35] Z. Chen, X. Li, J. Wang, L. Tao, M. Long, S.-J. Liang, et al., Synergistic effects of plasmonics and electron trapping in graphene short-wave infrared photodetectors with ultrahigh responsivity, ACS Nano 11 (2017) 430–437.
[36] J. Shen, X. Liu, X. Song, X. Li, J. Wang, Q. Zhou, et al., High-performance Schottky heterojunction photodetector with directly grown graphene nanowalls as electrodes, Nanoscale 9 (2017) 6020–6025.
[37] X. An, F. Liu, Y.J. Jung, S. Kar, Tunable graphene-silicon heterojunctions for ultrasensitive photodetection, Nano Lett. 13 (2013) 909–916.
[38] L. Qian, Y. Sun, M. Wu, D. Xie, L. Ding, G. Shi, A solution-processed high-performance phototransistor based on a perovskite composite with

chemically modified graphenes, Adv. Mater. 29 (2017) 1606175.
[39] D. Shao, M. Yu, H. Sun, T. Hu, J. Lian, S. Sawyer, High responsivity, fast ultraviolet photodetector fabricated from ZnO nanoparticle-graphene core-shell structures, Nanoscale 5 (2013) 3664–3667.
[40] J. Wu, Z. Yang, C. Qiu, Y. Zhang, Z. Wu, J. Yang, et al., Enhanced performance of a graphene/GaAs self-driven near-infrared photodetector with upconversion nanoparticles, Nanoscale 10 (2018) 8023–8030.
[41] W.J. Yu, Y. Liu, H. Zhou, A. Yin, Z. Li, Y. Huang, et al., Highly efficient gate-tunable photocurrent generation in vertical heterostructures of layered materials, Nat. Nanotechnol. 8 (2013) 952–958.